Journal of Materials Chemistry

Cite this: J. Mater. Chem., 2011, 21, 11244

www.rsc.org/materials

PAPER

Synthesis of magnetic, fluorescent and mesoporous core-shell-structured nanoparticles for imaging, targeting and photodynamic therapy†

Fang Wang,[a] Xiaolan Chen,*[a] Zengxia Zhao,[a] Shaoheng Tang,[a] Xiaoqing Huang,[a] Chenghong Lin,[b] Congbo Cai[b] and Nanfeng Zheng*[a]

Received 21st January 2011, Accepted 20th May 2011
DOI: 10.1039/c1jm10329f

A synthetic method to prepare novel multifunctional core-shell-structured mesoporous silica nanoparticles for simultaneous magnetic resonance (MR) and fluorescence imaging, cell targeting and photosensitization treatment has been developed. Superparamagnetic magnetite nanoparticles and fluorescent dyes are co-encapsulated inside nonporous silica nanoparticles as the core to provide dual-imaging capabilities (MR and optical). The photosensitizer molecules, tetra-substituted carboxyl aluminum phthalocyanine (AlC_4Pc), are covalently linked to the mesoporous silica shell and exhibit excellent photo-oxidation efficiency. The surface modification of the core-shell silica nanoparticles with folic acid enhances the delivery of photosensitizers to the targeting cancer cells that overexpress the folate receptor, and thereby decreases their toxicity to the surrounding normal tissues. These unique advantages make the prepared multifunctional core-shell silica nanoparticles promising for cancer diagnosis and therapy.

1. Introduction

Photodynamic therapy (PDT) is now well established as a technique for cancer treatment.[1–3] Typically, photosensitizers (PSs) are delivered to target cells or tissues either passively or actively and are irradiated with a laser. Upon irradiation, the activated PSs transfer the energy to ground-state oxygen to generate reactive oxygen species (ROS) that can kill the surrounding cancer cells.[4] The following three criteria must be met for an efficient PDT: (1) the PS should be highly specific to the targets in order to diminish the damage to normal tissues; (2) the local concentration of PS within diseased tissue is high enough to produce adequate singlet oxygen; and (3) there is adequate oxygen permeability/perfusion in the region of disease, which directly correlates to the subsequent photo-oxidation reaction efficiency.[5] To achieve a high PDT efficacy, the ability of PS to enter cells is critical. To date, various carriers, including oil dispersions, liposomes, low-density lipoproteins, polymeric micelles, gold nanoparticles, semiconductor quantum dots, iron oxide nanoparticles and silica nanoparticles, have been demonstrated with effective delivery of PSs.[6–20] These colloidal carriers not only display enhanced PSs loading capability and improve the reactivity of PSs, but can also be tailored to the appropriate size for a localized accumulation at the tumor site due to the "enhanced permeability and retention effect".[2,21] Furthermore, their surfaces can be modified with special targeting moieties such as antibodies, folate and aptamers for site-specific behavior.[17] Among the various delivery vehicles, mesoporous silica nanoparticles (MSNs) hold the promise to be a highly efficient PDT drug delivery platform owing to their attractive features such as uniform pore size, large surface area and high accessible pore volume, ease of chemical modification, excellent biocompatibility and avid uptake by cells.[22–26] The porous structure of MSNs not only permits the accommodation of a large quantity of PSs, but also helps to enhance the permeability of oxygen and generate singlet oxygen, which is essential for PDT. However, the reports on the applications of MSNs as PSs vehicles are rare.[27–30]

Moreover, the accurate localization of PS-containing nanoparticles in cells or target tissues is very important for effective PDT. It will offer a powerful guidance for site-directed

[a]*State Key Laboratory for Physical Chemistry of Solid Surfaces and Department of Chemistry, Xiamen University, College of Chemistry and Chemical Engineering, Xiamen, 361005, China. E-mail: chenxl@xmu.edu.cn; Tel: +86 -592-2186821; nfzheng@xmu.edu.cn*

[b]*Departments of Physics and Communications Engineering, Xiamen University, Xiamen, 361005, China*

† Electronic supplementary information (ESI) available: The structure of AlC_4Pc, XRD pattern of Fe_3O_4 nanoparticles, TEM images of Fe_3O_4@SiO_2(F)@*meso*-SiO_2(P) with different amounts of TEOS, DLS and dispersion stability of Fe_3O_4@SiO_2(F)@*meso*-SiO_2(P) and Fe_3O_4@SiO_2(F)@*meso*-SiO_2(P)-Folate nanoparticles in water and other buffers, Fluorescence spectra of Fe_3O_4@SiO_2(F)@*meso*-SiO_2(P) under 488 nm excitation after different periods of irradiation with a 660 nm laser beam, The viability of human hepatocyte cells incubated with Fe_3O_4@SiO_2(F)@*meso*-SiO_2(P) at different concentrations, the zeta-potential of Fe_3O_4@SiO_2(F)@*meso*-SiO_2(P) and Fe_3O_4@SiO_2(F)@*meso*-SiO_2(P)-Folate nanoparticles at different pH, Optical imagings of HeLa cells stained with Trypan blue after different treatment. The FT-IR spectra of Fe_3O_4@SiO_2(F)@*meso*-SiO_2(P) and Fe_3O_4@SiO_2(F)@*meso*-SiO_2(P)-Folate. See DOI: 10.1039/c1jm10329f

irradiation of target diseased tissues without causing damage to the healthy tissues.[31] Recently, optical imaging probes have been incorporated into MSNs along with PSs to offer dual capability of imaging and therapy.[28–30] Optical imaging can provide the highest sensitivity and obtain detailed information at subcellular levels,[32] which allow accurate targeting and simultaneous phototherapy treatment. However, optical imaging still lacks the full capability to obtain anatomic and physiological details *in vivo*. Compared to optical imaging, magnetic resonance imaging (MRI) offers an excellent spatial resolution and depth for *in vivo* imaging, which can provide an anatomic reference. However, MRI suffers from limited sensitivity and lacks resolution for imaging at the cellular level.[33] A combination of optical imaging and MRI leads to the development of bimodal imaging probes that can provide the high sensitivity and resolution of fluorescence imaging, as well as the noninvasive and real-time monitoring abilities of magnetic resonance imaging, allowing accurate following the distribution of PSs *in vivo* and monitoring the therapeutic efficiency of photodynamic therapy (PDT). However, the application of multifunctional MSNs as photosensitizing vehicles that provides both MR and fluorescence imaging diagnosis and photodynamic therapy has not been satisfied explored.

Herein, we report a facile strategy to fabricate discrete, monodisperse and size-controllable core-shell nanoparticles integrating the capabilities of MR imaging, fluorescent imaging, cancer cell-specific delivery and photodynamic therapy. While the core of the nanoparticles consists of a single Fe_3O_4 nanoparticle encapsulated in fluorescent dyes co-doped nonporous silica, their shell is made from ordered mesoporous silica containing PSs. The nanoparticles are further surface-functionalized by folic acid to gain the targeting capacity. Fluorescein isothiocyanate (FITC) was chosen as the fluorescence imaging agent to be covalently incorporated into the silica core which can isolate the dyes from the external environment and thus protect the dyes from photobleaching. The photosensitizer molecules of tetra-substituted carboxyl aluminum phthalocyanine (AlC_4Pc, Figure S1, ESI†) were covalently linked to the mesoporous silica. In the case of being physically entrapped inside the silica network, the PS can be prematurely released from the carrier vehicles while in systemic circulation, leading to a reduced efficiency of PDT treatment.[34] The covalent coupling of photosensitizer molecules in the rigid porous structure in our core-shell carriers helps to obviate the degradation of PS in harsh biological environments, and overcome their premature release. Furthermore, the mesoporous structure of the shell permits the easy diffusion of O_2 to interact with the PS molecules for ROS generation. Together with the MRI and fluorescence imaging capabilities of these nanoparticles in living cells, we have also evaluated their PDT potential in the treatment of cancer cells.

2. Experimental

2.1. Chemicals

Oleic acid, oleylamine, benzyl alcohol, tetraethoxysilane (TEOS), 3-aminopropyltriethoxysilane (APTES) and ethyl-[3-(dimethylamino)propyl]-carbodiimide hydrochloride (EDC) were purchased from Aldrich Chemical Co. Iron(III) acetylacetonate ($Fe(acac)_3$) was obtained from Strem Chemical Inc. Brij 56 were purchased from Alfa Aesar. Human hepatoma cells (QGY-7703), human hepatocytes (QSG-7701) and HeLa cells were purchased from cell storeroom of Chinese Academy of Science. RPMI 1640 cell culture medium, bovine serum albumin (BSA) and Penicillin-Streptomycin compound were purchased from Hyclone Laboratories Inc. 3-[4,5-dimethylthiazol-2-yl]-2,5-diphenyltetrazolium bromide (MTT), Fluorescein isothiocyanate (FITC), 1,3-diphenylisobenzofuran (DPBF) and *N*-hydroxysuccinimide (NHS) were purchased from Sigma. Tetra-substituted carboxyl aluminum phthalocyanine (AlC_4Pc) was synthesized and purified according to a method in the literature.[35] The water used in all experiments was ultrapure. All other chemicals were of analytical-reagent grade and used without further purification.

2.2. Synthesis of Fe_3O_4 nanoparticles

The magnetic particles were prepared through a solvothermal reaction.[36] Briefly, 0.353 g of $Fe(acac)_3$, 1.5 mL oleic acid and 1.5 mL oleylamine were added to 10.0 mL of benzyl alcohol under magnetic stirring. The obtained homogeneous yellow solution was transferred to a Teflon-lined stainless-steel autoclave and sealed to heat at 180 °C. After reacting for 10 h, the autoclave was cooled to room temperature. The obtained black magnetite particles were washed with ethanol three times, and then redispersed into 9.0 mL cyclohexane for further use.

2.3. Synthesis of Fe_3O_4@SiO_2 or Fe_3O_4@SiO_2(F) nanoparticles

The nonporous silica layer was coated on the Fe_3O_4 nanoparticles by a reverse micelle method. 2 mg of FITC was reacted with 15 μL of APTES in 1.0 mL of ethanol under dark conditions for 24 h. The prepared FITC–APTES stock solution was kept at 4 °C. In a typical procedure, 1.4 g of Brij56, 0.75 mL of the above cyclohexane solution of Fe_3O_4 nanoparticles, 0.075 mL H_2O and 0.28 mL concentrated ammonia were added to 5.625 mL cyclohexane. After stirring for 30 min, 0.75 mL of TEOS, or 0.5 mL of FITC–APTES and 0.75 mL of TEOS were added. The reaction mixture was further stirred for 8 h at 50 °C in a water bath in the dark. The particles were separated and washed with ethanol for a few times. The obtained Fe_3O_4@SiO_2 or Fe_3O_4@SiO_2(F) magnetic nanoparticles were stored for further use.

2.4. Synthesis of Fe_3O_4@SiO_2@*meso*-SiO_2(P) and Fe_3O_4@SiO_2(F)@*meso*-SiO_2(P) nanoparticles

Mesoporous silica was further coated onto the Fe_3O_4@SiO_2 or Fe_3O_4@SiO_2(F). The photosensitizer AlC_4Pc–APTES conjugate was prepared in advance. In a flask, 2 mg of AlC_4Pc and 10 μL of APTES were mixed in 1 mL of DMSO. Next, 3.0 mg of EDC and 2.0 mg of NHS were added into the mixture and stirred for 24 h at room temperature. The obtained solution was directly used without further treatment. The Fe_3O_4@SiO_2@*meso*-SiO_2(P) or Fe_3O_4@SiO_2(F)@*meso*-SiO_2(P) nanoparticles were prepared by a modified Stöber sol–gel process.[37] Typically, 0.2 g Fe_3O_4@SiO_2 or Fe_3O_4@SiO_2(F) nanoparticles, 0.17 g CTAB, 0.5 mL concentrated ammonia and 25 mL ethanol were added to 54 mL H_2O. After being ultrasonicated for 10 min, 1.0 mL of the

AlC_4Pc–APTES solution and 0.3 mL of TEOS were added. The reaction mixture was further stirred for 8 h at room temperature. The particles were separated and washed twice with ethanol. Finally, the nanospheres were redispersed in 60 mL of acetone and refluxed at 80 °C for 24 h to remove the template CTAB. The extraction was repeated twice, and the nanospheres were then centrifuged and washed with ethanol. The amount of bound AlC_4Pc was determined indirectly by the difference between the amount of AlC_4Pc introduced into the sol–gel reaction and the amount of AlC_4Pc in the washing solutions through UV-Vis spectroscopy; the amount of AlC_4Pc conjugated into the mesoporous silica was about 0.51 wt%.

2.5. Surface modification of the Fe_3O_4@SiO_2(F)@*meso*-SiO_2(P) nanoparticles with folic acid

To attach folic acid to the Fe_3O_4@SiO_2(F)@*meso*-SiO_2(P), the folate–APTES conjugate was prepared in advance. 1 mg of folic acid and 5 μL of APTES were mixed in 1 mL of DMSO which contains 30 mg of NHS and 50 mg of EDC and stirred for 2 h. Then, the folate–APTES conjugate was added to a flask containing 4 mL of toluene and 1 mL of Fe_3O_4@SiO_2(F)@*meso*-SiO_2(P) solution (20 mg nanoparticles suspended in 1 mL DMSO) and stirred for 20 h at room temperature. The nanoparticles were then centrifuged and washed with toluene, and dispersed in ethanol.

2.6. Detection of singlet oxygen ($^1O_2$)

The singlet oxygen ($^1O_2$) generation capabilities of the Fe_3O_4@SiO_2@*meso*-SiO_2(P), Fe_3O_4@SiO_2(F)@*meso*-SiO_2(P) and free AlC_4Pc were determined by a chemical method, using 1,3-diphenylisobenzofuran (DPBF) as a singlet oxygen sensor.[38] DPBF reacts irreversibly with $^1O_2$ which causes a decrease in the DPBF absorption at 400 nm. In a typical experiment, 50 μL of DPBF (1.5 mg mL^{-1} in acetonitrile) was added into 2 mL of 1.5 mg mL^{-1} nanoparticles solution in acetonitrile, while the control used DPBF only in acetonitrile and free AlC_4Pc with DPBF in acetonitrile. The solutions were then irradiated with a 660 nm laser source, and their optical densities at 400 nm were recorded at 0, 5, 10, 15, 20, 25, 30, 36, 41, 60, 80, 100, 120 s, respectively, using the DU-7400 spectrophotometer.

2.7. Fluorescence imaging and magnetic resonance imaging (MRI)

Human hepatoma cells (QGY-7703), human hepatocytes (QSG-7701) were cultured in RPMI 1640 medium supplemented with 10% calf serum, 100 U mL^{-1} penicillin and 100 μg mL^{-1} streptomycin in 37 °C, 5% CO_2. The cellular uptake of the nanoparticles was confirmed by fluorescence microscopy. The cells were plated in a 24 well-plate (Nunc ™) with a density of $\sim 0.5 \times 10^4$ cells per well. After incubation in fresh medium for 24 h, cells were incubated with 0.5 mL of the medium containing 200 μg mL^{-1} nanoparticles for 8 h. The cell medium was removed, and the cells were washed three times with 0.5 mL PBS to remove the nanoparticles that did not enter the cells. The green fluorescence emission in cells was detected under the fluorescence microscopy. For the experiments to observe the MR contrast effect of the nanoparticles within the cells, human hepatoma cells (QGY-7703) were incubated with either the Fe_3O_4@SiO_2(F)@*meso*-SiO_2(P) or plain mesoporous silica nanoparticles under similar conditions as mentioned above. The adherent cells were detached from the plate by treatment with trypsin-EDTA and placed in 0.5 mL cell medium for MR imaging. Each tube contained approximately 10^5 cells.

2.8. Cell viability assay

The *in vitro* cytotoxicity was measured by using the MTT assay in human hepatocytes. Cells were initially seeded into a 96-well cell-culture plate (Nunc ™) at $\sim 10^4$ per well and then incubated for 24 h at 37 °C under 5% CO_2. RPMI 1640 solutions of nanoparticles (0.2 mL per well) at concentrations of 0, 50, 100, 200, 400, 800 μg mL^{-1} were added to the wells. The cells were further incubated for 24 h at 37 °C under 5% CO_2. The cells were washed three times with 0.2 mL PBS to remove the unbound nanoparticles. Subsequently, 0.2 mL RPMI 1640 and 25 μL MTT (5 mg mL^{-1}) were added to each well and incubated for an additional 4 h at 37 °C under 5% CO_2. Then the medium solution was replaced by 0.15 mL dimethylsulfoxide (DMSO) solution. After 10 min, the optical density at 490 nm (absorption value) of each well was measured on a Tecan Infinite M 200 monochromator-based multifunction microplate reader. The corresponding nanoparticles with cells but not treated by MTT were used as controls. The cells vitality after labeling was compared with that of unlabeled cells and expressed as the relative ratio.

2.9. Photodynamic effect of the nanoparticles on human hepatoma cells

For MTT assay, human hepatoma cells were seeded in a 96-well plate at a density of 10^4 cells per well for 24 h. Then RPMI 1640 cell medium containing different concentrations of Fe_3O_4@SiO_2(F)@*meso*-SiO_2(P) nanoparticles were added to the wells (0.2 mL per well, 0, 50, 100, 200, 400, 800 μg mL^{-1}). After incubation for 14 h, the cells were washed three times with 0.2 mL PBS to remove the unbound nanoparticles. Then 0.2 mL PBS was added and the cells were exposed to a 660 nm laser with a power density of 75 mW cm^{-2} for 5 min. The cell viability was measured by MTT assay mentioned above and expressed as a percentage of the control.

For optical imaging, human hepatoma cells were seeded in a 24-well plate at a density of 10^5 cells per well for 24 h. Then the medium was replaced by cell medium containing 200 μg mL^{-1} of Fe_3O_4@SiO_2(F)@*meso*-SiO_2(P) (0.5 mL per well). After incubation for 14 h, the cells were washed three times with 0.5 mL PBS to remove the unbound nanoparticles. Then 0.5 mL PBS was added and the cells were exposed to a 660 nm laser with a power density of 75 mW cm^{-2} for 2.5 and 10 min, respectively. After trypan blue staining, the optical imaging was performed by fluorescence microscopy.

2.10. Targeting of HeLa cells by Fe_3O_4@SiO_2(F)@*meso*-SiO_2(P)-Folate nanoparticles

HeLa cells were cultured in RPMI 1640 medium supplemented with 10% calf serum, 100 U mL^{-1} penicillin and 100 μg mL^{-1} streptomycin in 37 °C, 5% CO_2. To study the cellular uptake of Fe_3O_4@SiO_2(F)@*meso*-SiO_2(P)-Folate, HeLa cells were seeded in 35 mm dishes at a density of about 5×10^4 cells per dish in

RPMI-1640. After incubation for 24 h, the culture medium was replaced by the same medium containing 200 μg mL^{-1} Fe_3O_4@SiO_2(F)@*meso*- SiO_2(P)-Folate nanoparticles or Fe_3O_4@SiO_2(F)@*meso*- SiO_2(P). After incubation for 8 h, the cell medium was removed, and the cells were washed three times with 1.0 mL PBS. The cells were then stained with DAPI solution before being monitored using an Olympus Fluoriew 1000 laser-scanning microscope. For flow cytometry analysis, HeLa cells were plated in 24 well-plate with a density of 5×10^4 cells per well. After incubation in the fresh RPMI 1640 medium for 24 h, cells were incubated with 0.5 mL of the medium containing 200 μg mL^{-1} Fe_3O_4@SiO_2(F)@*meso*-SiO_2(P)-Folate nanoparticles for 8 h. The cell medium was removed, and the cells were washed three times with 0.5 mL PBS buffer solution. The adherent cells were detached from the plate by treatment with trypsin-EDTA, washed and then suspended in 0.5 mL PBS buffer solution for flow cytometry. For MTT assay of the PDT effects on HeLa cells, the procedure was similar to that described previously.

2.11. Characterization

The size and morphologies of nanoparticles were determined at 300 kV using a TECNAI F-30 high-resolution transmission electron microscopy. Powder X-ray diffraction (XRD) measurements were taken with a Rigaku D/Max rC X-ray diffractometer with a rotating target. Magnetic characterization of Fe_3O_4 nanoparticles was performed by a superconducting quantum interference device (Magnetic Property Measurement System XL-7, Quantum Design). Fluorescence spectra were recorded with a Hitachi F-4500 fluorescence spectrofluorimeter. UV-Visible absorption spectra were measured using a Beckman DU-7400 ultraviolet-visible diode array spectrophotometer. A MRL-III-660 laser (100 mW, Changchun New Industries Optoelectronics Tech. Co. Ltd.) was used as the irradiation source. Dynamic light scattering (DLS) and zeta potential experiments were carried out on a Nano-ZS (Malvern Instruments). Fluorescence imaging was performed on a Nikon eclipse Ti-U fluorescence microscope with a C-FL Epi-Fl Filter Block FITC consisting of excitation filter Ex 465–495, dichroic mirror DM 505, and barrier filter BA 515–555. Confocal fluorescence imaging of cells was performed with an Olympus Fluoriew 1000 laser-scanning microscope. Excitation of FITC was carried out with an Ar laser at $\lambda = 488$ nm, and emissions were collected in the range $\lambda = 505$–600 nm. DAPI was excited by a 405 nm laser and the emissions were collected in the range $\lambda = 420$–480 nm. MRI experiments were performed on a Varian 7.0-T MR system. An extremity coil was used for the data acquisition, and the pulse sequence used was a T_2-weighted turbo spin-echo sequence with the following parameters: TR = 3000 ms, slice thickness = 2 mm, TE = 70 ms, field of view = 45 × 45 mm, number of acquisitions = 1. Flow cytometry (Becton Dickinson).

3. Results and discussion

3.1. Synthesis and characteristics of the multifunctional nanoparticles

The multifunctional core-shell nanoparticles were prepared by a multistep process (Scheme 1) (see Experimental section for details). In brief, monodisperse superparamagnetic Fe_3O_4 nanoparticles were first prepared using the modified solvothermal method.[36] The prepared Fe_3O_4 nanoparticles were then coated with a layer of nonporous silica to form Fe_3O_4@silica spheres (denoted as Fe_3O_4@SiO_2) *via* a reverse micelle method. To covalently incorporate FITC into the Fe_3O_4@SiO_2 particles, FITC was treated with 3-aminopropyltriethoxysilane (APTES) and then co-hydrolyzed with tetraethyl orthosilicate (TEOS) during the reverse micelle encapsulation process to yield the fluorescent Fe_3O_4@SiO_2(F) particles. After being separated and cleaned, the Fe_3O_4@SiO_2(F) particles were dispersed in ethanol for the subsequent coating of a mesoporous silica layer. The coating of such a mesoporous SiO_2 was achieved by base-catalyzed hydrolysis of TEOS in the presence of cetyltrimethylammonium bromide (CTAB).[37] To covalently bind the photosensitizer molecules (AlC_4Pc) in the mesoporous silica layer, AlC_4Pc was treated with APTES in advance to form an APTES-AlC_4Pc conjugate. The conjugate was then supplied together with TEOS during the coating process. The resultant core-shell composite was designated as Fe_3O_4@SiO_2(F)@*meso*-SiO_2(P). An acetone extraction treatment was then applied to remove the surfactant from the mesoporous shell of the composite. Finally, the targeting ligands, folic acid, which can recognize the over-expressed α-folate receptor in many cancer cells, were covalently anchored on the surface of Fe_3O_4@SiO_2(F)@*meso*-SiO_2(P) nanoparticles to produce Fe_3O_4@SiO_2(F)@*meso*-SiO_2(P)-Folate particles.

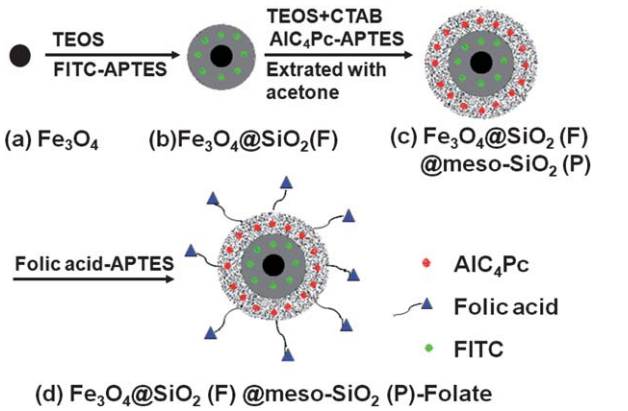

Scheme 1 Synthetic procedure of Fe_3O_4@SiO_2(F)@*meso*-SiO_2(P)-Folate nanoparticles.

As shown in Fig. 1a, the prepared monodisperse hydrophobic Fe_3O_4 nanoparticles have an average size of ~6 nm. In the X-ray diffraction (XRD) pattern, the main peaks match well with the standard PDF data of magnetite Fe_3O_4 (JCPDS No. 01-089-0691) (Figure S2, ESI†). Using the reverse micelle system of Brij56-water-cyclohexane, Fe_3O_4 were successfully encapsulated within SiO_2 in a one-in-one fashion (Fig. 1b). The prepared Fe_3O_4@SiO_2 nanoparticles had a uniform diameter of 40 ± 5 nm. As illustrated in the TEM image (Fig. 1c), a uniform layer of mesoporous silica with a thickness of ~ 9 nm was coated onto the Fe_3O_4@SiO_2(F) by hydrolysis of TEOS in the presence of CTAB. The thickness of the mesoporous silica shell is tunable by varying the amount of TEOS (Figure S3, ESI†). After template removal, the mesoporous feature in the core-shell composite was

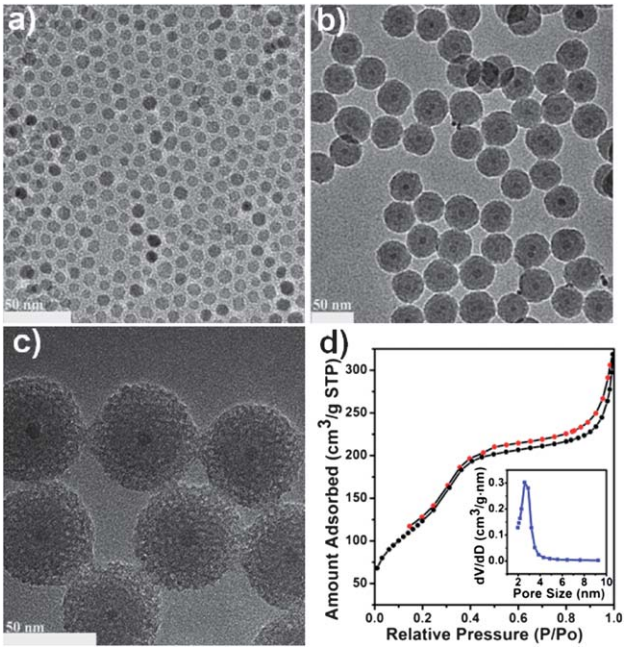

Fig. 1 TEM images of a) Fe_3O_4, b) Fe_3O_4@SiO_2(F) and c) Fe_3O_4@SiO_2(F)@*meso*-SiO_2(P). d) N_2 adsorption/desorption isotherms (77 K) and pore size distribution (inset) of Fe_3O_4@SiO_2(F)@*meso*-SiO_2(P).

confirmed by the N_2 adsorption/desorption measurements (Fig. 1d). The Brunauer–Emmett–Teller (BET) surface area and the total pore volume of the Fe_3O_4@SiO_2(F)@*meso*-SiO_2(P) composite were measured to be 455 m^2 g^{-1} and 0.99 cm^3 g^{-1}, respectively. The Brunauer–Joyner–Halenda (BJH) pore-size distribution indicates that the Fe_3O_4@SiO_2(F)@*meso*-SiO_2(P) nanoparticles have uniform mesopores with an average pore size of 2.5 nm. The overall small particle size (about 50 nm) and the uniform mesoporous pore holes give these nanoparticles the potential for imaging and photodynamic therapy applications.

3.2. Cancer cells imaging using the multifunctional nanoparticles

Superparamagnetic nanoparticles are often used as contrasting agents in MRI. The magnetic measurement of the Fe_3O_4@SiO_2(F)@*meso*-SiO_2(P) nanoparticles at 300 K displays no hysteresis (Fig. 2a), indicating that they are super-paramagnetic and favorable for T_2 MR contrast agents.[38] The T_2 relaxivity (r_2, the efficiency of a contrast agent) of the Fe_3O_4@SiO_2(F)@*meso*-SiO_2(P) nanoparticles was determined to be 194.66 mM^{-1} S^{-1} (The Fe content of the Fe_3O_4@SiO_2(F)@*meso*-SiO_2(P) was determined by inductively coupled plasma-atomic emission spectroscopy (ICP-AES)) (Fig. 2b). In order to evaluate the contrast effect of these nanoparticles inside the cells, human hepatoma cells (QGY-7703) were first incubated with different concentrations of nanoparticles for 8 h before being washed and re-collected in 0.5 mL RPMI cell medium in 0.6 mL centrifuge tubes. The untreated cells and the cells treated with plain mesoporous silica nanoparticles (without the magnetite) were used as controls. As shown in Fig. 2c, the tubes containing the control samples are fairly bright, whereas the brightness of the tubes containing the cells treated with the

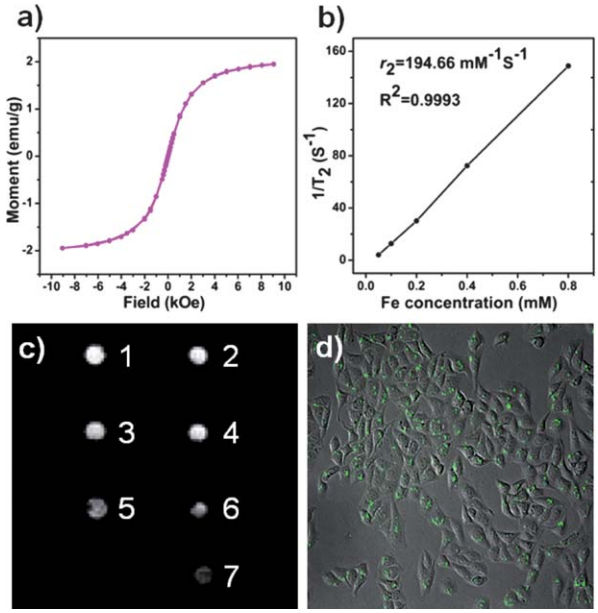

Fig. 2 a) Field-dependent magnetization at 300 K. b) T_2 relaxivity plot of an aqueous suspension of Fe_3O_4@SiO_2(F)@*meso*-SiO_2(P) measured at 7.0 T, the slope indicates the T_2 relaxivity coefficient (r_2). c) T_2-weighted MR images of human hepatoma cells that were treated with Fe_3O_4@SiO_2(F)@*meso*-SiO_2(P) at different concentrations appeared dark compared to the other samples, (1) RPMI medium; (2) plain mesoporous silica nanoparticles (800 μg mL^{-1}), and Fe_3O_4@SiO_2(F)@*meso*-SiO_2(P) at (3) 50, (4) 100, (5) 200, (6) 400 and (7) 800 μg mL^{-1}. d) Fluorescence image showing the uptake of Fe_3O_4@SiO_2(F)@*meso*-SiO_2(P) by hepatoma cells.

Fe_3O_4@SiO_2(F)@*meso*-SiO_2(P) nanoparticles was reduced as the concentration of the nanoparticles was increased because of the decrease in T_2 relaxation. These results indicate that the Fe_3O_4@SiO_2(F)@*meso*-SiO_2(P) nanoparticles can be used as MR contrast agents *in vitro*.

For fluorescence imaging, FITC was incorporated covalently into the nonporous inner layer silica walls of the Fe_3O_4@SiO_2(F)@*meso*-SiO_2(P) nanoparticles using a co-condensation method in the preparation process. The introduction of fluorescence functionality made it possible to directly monitor the cellular uptake of the nanoparticles by fluorescence microscopy. After QGY-7703 cells were incubated with the nanoparticles for 8 h, the unbound nanoparticles were washed away and the living cells were imaged using a fluorescence microscope. As shown in Fig. 2d, the fluorescence from the nanoparticles was readily observed within the cells. In comparison, under similar imaging conditions the control cells incubated without the nanoparticles showed no fluorescence.

3.3. Photosensitizers loading and singlet oxygen generation

With FITC in the solid SiO_2 core and AlC_4Pc covalently bound in the mesoporous silica shell, as shown in Fig. 3a, the prepared Fe_3O_4@SiO_2(F)@*meso*-SiO_2(P) particles display the adsorption features of both FITC and AlC_4Pc. Besides an obvious absorption of FITC at 480 nm, both Soret and Q-band absorptions of AlC_4Pc at 350 and 685 nm, respectively, were observed in Fe_3O_4@SiO_2(F)@*meso*-SiO_2(P). The presence of the Soret and

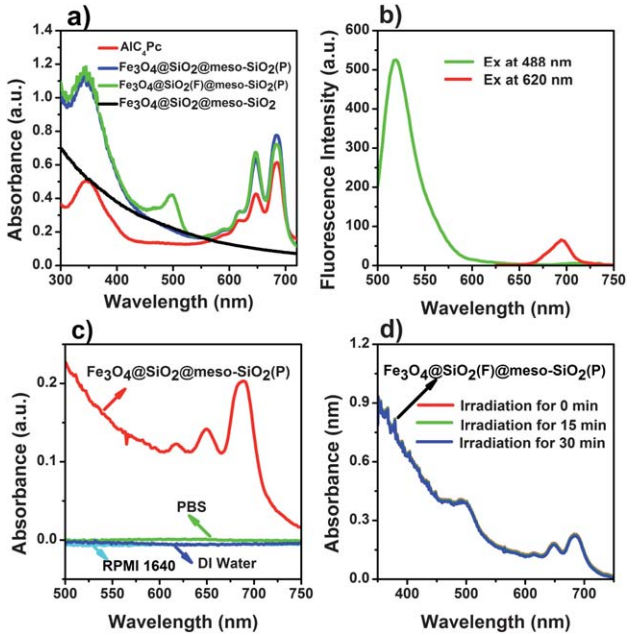

Fig. 3 a) Absorption spectra of Fe_3O_4@SiO_2(F)@*meso*-SiO_2(P), Fe_3O_4@SiO_2@*meso*-SiO_2(P), Fe_3O_4@SiO_2@*meso*-SiO_2 and free AlC_4Pc. b) Emission spectra of Fe_3O_4@SiO_2(F)@*meso*-SiO_2(P) under excitation wavelength at 488 and 620 nm, respectively. c) Fe_3O_4@SiO_2@*meso*-SiO_2(P) were dispersed in DI water, PBS buffer and RPMI 1640 cell culture medium, respectively, for 10 days. The nanoparticles were then centrifuged down and UV-Vis absorption spectra of the supernatants were measured. d) Absorption spectra of Fe_3O_4@SiO_2(F)@*meso*-SiO_2(P) dispersed in RPMI 1640 cell medium for different times of irradiation with a 660 nm laser source (75 mW cm^{-2}).

Q-band absorptions features similar to free AlC_4Pc molecules suggested the absence of heavy aggregation of AlC_4Pc molecules in both Fe_3O_4@SiO_2@*meso*-SiO_2(P) and Fe_3O_4@SiO_2(F)@*meso*-SiO_2(P) particles. In order to investigate the possible influence of FITC on the optical properties of the photosensitizer, the fluorescence emission spectra of Fe_3O_4@SiO_2(F)@*meso*-SiO_2(P) dispersed in water were recorded using various excitation wavelengths. When excited at 488 nm (the absorption of FITC), the nanoparticles exhibited only one emission peak at 520 nm corresponding to that from fluorescein. When the excitation was changed to 620 nm, the emission spectrum was dominated by the emission of AlC_4Pc with a peak at 695 nm (Fig. 3b). Under excitation of different wavelengths, Fe_3O_4@SiO_2(F)@*meso*-SiO_2(P) display different emission spectra, suggesting that these nanoparticles could be used for both imaging and photodynamic therapy by switching the wavelength to allow the light absorption by either FITC or AlC_4Pc. Our photosensitization experiments were performed at 660 nm to ensure that the light was absorbed only by AlC_4Pc for the photosensitization process.

Before photosensitization studies, the leakage of AlC_4Pc from the nanoparticles were investigated by soaking the nanoparticles in deionized (DI) water, phosphate-buffered saline (PBS) solution and RPMI 1640 cell culture medium, respectively, for ten days. After centrifuging, the supernatants were subjected to UV-Vis adsorption measurements. As illustrated in Fig. 3c, no detectable dye leakage from the nanoparticles was observed after ten days of incubation in all three solutions, suggesting that Fe_3O_4@SiO_2@*meso*-SiO_2(P) nanoparticles are very stable against dye leaching. The Fe_3O_4@SiO_2(F)@*meso*-SiO_2(P) nanoparticles also demonstrated good dispersion stability in water, PBS and cell medium (Figure S4, ESI†), respectively. The effective hydrodynamic diameter measured by dynamic light scattering (DLS) was about 56 nm (Figure S4b, ESI†), confirming that Fe_3O_4@SiO_2(F)@*meso*-SiO_2(P) nanoparticles are well-dispersed in water. When the nanoparticles were stored in water and PBS for a week (Figure S4c, ESI†), or 10 h in cell medium (Figure S4d, ESI†), no significant decrease of absorption intensity was observed. In addition, the photobleaching tests of the Fe_3O_4@SiO_2(F)@*meso*-SiO_2(P) nanoparticles were also performed (Fig. 3d). After the nanoparticles were dispersed in RPMI 1640 cell medium, the nanoparticle solutions were irradiated by a 660 nm laser (75 mW cm^{-2}) for 15 and 30 min, respectively. The experimental results indicated that the absorption spectra of the nanoparticle solution didn't show any obvious change after 15 and 30 min irradiation. This further suggests that our Fe_3O_4@SiO_2(F)@*meso*-SiO_2(P) nanoparticles are very stable against photobleaching. All these will help with the long-term studies in which nanoparticles need to be monitored over days or even longer.

The PDT-induced cytotoxicity of type II PS is attributed to the generation of singlet oxygen ($^1O_2$).[33] As a potential second-generation PS displaying strong absorption in the red visible region, AlC_4Pc has a good selectivity for tumors targets and enhanced PDT-induced cytotoxic efficiency due to its high efficiency of singlet-oxygen photogeneration.[39,40] To investigate the effectiveness of Fe_3O_4@SiO_2@*meso*-SiO_2(P) in generating $^1O_2$ upon light irradiation, we used its reaction with 1,3-diphenylisobenzofuran (DPBF) as an indicator. The reaction results in the absorption decrease of DPBF at 400 nm.[41] Fig. 4a shows the absorption spectra of DPBF in the presence of Fe_3O_4@SiO_2@*meso*-SiO_2(P) nanoparticles after different times of irradiation with a 660 nm laser source at 75 mW cm^{-2}. As

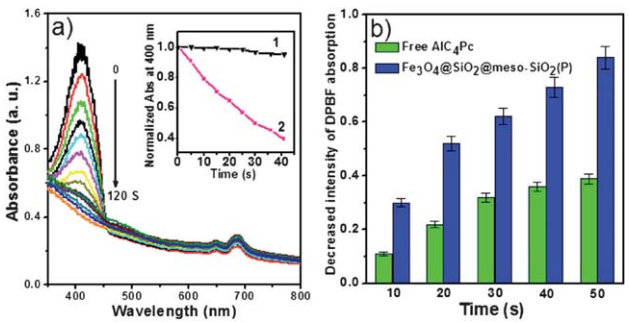

Fig. 4 a) Absorption spectra of Fe_3O_4@SiO_2@*meso*-SiO_2(P) in the presence of DPBF after different times of irradiation with a 660 nm laser source. The concentration of Fe_3O_4@SiO_2@*meso*-SiO_2(P) is 1.5 mg mL^{-1}. Inset: Decay curves of absorption of DPBF at 400 nm as a function of irradiation time in the presence (Trace 2) and absence (Trace 1) of Fe_3O_4@SiO_2@*meso*-SiO_2(P). b) Time-dependent photooxidation of DPBF caused by single oxygen generated in acetonitrile by using Fe_3O_4@SiO_2@*meso*-SiO_2(P) and the same amount of AlC_4Pc in homogeneous solution. The concentrations for loading AlC_4Pc and free AlC_4Pc is 1.0×10^{-5} mol L^{-1}, respectively.

illustrated in the inset of Fig. 4a, while no obvious absorption decrease was observed in the absence of Fe_3O_4@SiO_2@*meso*-SiO_2(P), the absorption at 400 nm continuously decreased with the irradiation time in the presence of Fe_3O_4@SiO_2@*meso*-SiO_2(P). The steep decrease of DPBF absorption implies the continuous generation of $^1O_2$ by irradiated Fe_3O_4@SiO_2@*meso*-SiO_2(P). It is worth noting that the AlC_4Pc-incorporated Fe_3O_4@SiO_2@*meso*-SiO_2(P) particles exhibited much higher activity in photo-oxidation DPBF than the same amount of free AlC_4Pc in solution (Fig. 4b). The enhanced activity by Fe_3O_4@SiO_2@*meso*-SiO_2(P) suggests that the mesoporous silica nanovehicle acts not only as a carrier for the photosensitizers but also as a nanoreactor to facilitate the photo-oxidation reaction, consistent with previous observations.[29] Even with the co-presence of FITC and AlC_4Pc, Fe_3O_4@SiO_2(F)@*meso*-SiO_2(P) exhibits the capability of $^1O_2$ generation similar to that of Fe_3O_4@SiO_2@*meso*-SiO_2(P) nanoparticles. More importantly, the fluorescence spectra of the doped FITC molecules were not affected during the $^1O_2$ photogeneration process (Figure S5, ESI†), suggesting that FITC molecules were well protected in the nonporous silica core and therefore not photo-oxidized by the generated $^1O_2$ during the photosensitization process. Without doubt, the solid core-mesoporous shell feature of the prepared Fe_3O_4@SiO_2(F)@*meso*-SiO_2(P) represents an ideal nanostructure to integrate PDT drugs together with imaging agents.

3.4. Laser-induced *in vitro* PDT effect on cancer cells

Before *in vitro* PDT studies in cells, we examined the biocompatibility of the Fe_3O_4@SiO_2(F)@*meso*-SiO_2(P) nanoparticles. The relative cell viabilities of human hepatocyte cells (QSG-7701) after 24 h incubation with different concentrations of nanoparticles were measured by the MTT assay. When the concentration of Fe_3O_4@SiO_2(F)@*meso*-SiO_2(P) nanoparticles was up to 800 μg mL^{-1}, the cell viability was still kept at more than 60% (Figure S6, ESI†), indicating that these nanoparticles are highly biocompatible. To investigate the PDT efficiency of Fe_3O_4@SiO_2(F)@*meso*-SiO_2(P), human hepatoma cells (QGY-7703) were first incubated with different concentrations of Fe_3O_4@SiO_2(F)@*meso*-SiO_2(P) nanoparticles for 14 h and then treated with or without laser (660 nm) irradiation. The MTT assay was used to assess the cell viabilities. After 5 min of continuous laser irradiation at 75 mW cm^{-2}, the viability of QGY-7703 incubated with 200 μg mL^{-1} nanoparticles was 28 ± 2%, significantly lower than those without irradiation (84 ± 4%) (Fig. 5). This result indicated that light plays a key role in killing tumor cells *in vitro*. When the concentration of Fe_3O_4@SiO_2(F)@*meso*-SiO_2(P) nanoparticles was increased beyond 200 μg mL^{-1}, the increment of photo-induced cytotoxicity in QGY-7703 slightly increased. However, the dark cytotoxicity of Fe_3O_4@SiO_2(F)@*meso*-SiO_2(P) in QGY-7703 was also further increased. We have therefore selected 200 μg mL^{-1} as the concentration of Fe_3O_4@SiO_2(F)@*meso*-SiO_2(P) for the time-dependent studies of the photo-induced cytotoxicity. After 14 h incubation with the nanoparticles, the cells were irradiated with a 660 nm laser (75 mW cm^{-2}) for 2.5 min and 10 min, respectively. The dead cells were then stained with trypan blue, a vitality dye that only stains the cell when the membrane is damaged. Microscopic images of QGY-7703 after different

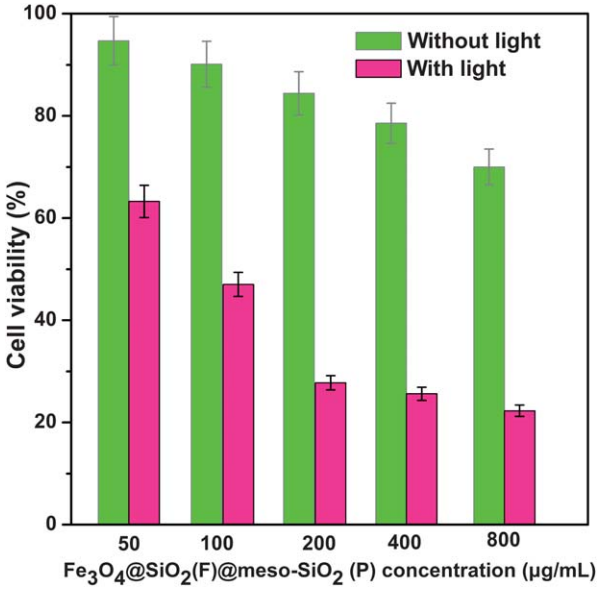

Fig. 5 The cytotoxicity of different concentrations of Fe_3O_4@SiO_2(F)@*meso*-SiO_2(P) on hepatoma cells with 5 min light exposure and without light irradiation. The concentrations of AlC_4Pc were 3.4 × 10^{-7}, 6.8 × 10^{-7},1.4 × 10^{-6},2.8 × 10^{-6}, 5.6 × 10^{-6} mol L^{-1}, respectively.

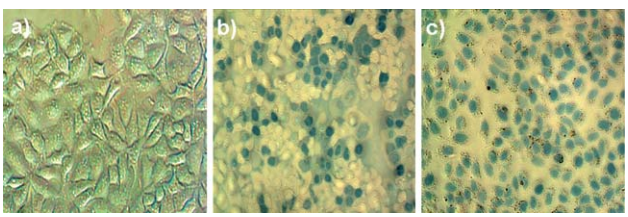

Fig. 6 Optical imaging of hepatoma cells stained with Trypan blue after different treatments: a) without nanoparticles and 10 min light exposure with 75 mW cm^{-2}; b) 200 μg mL^{-1} Fe_3O_4@SiO_2(F)@*meso*-SiO_2(P) and 2.5 min light exposure with 75 mW cm^{-2}; c) 200 μg mL^{-1} Fe_3O_4@SiO_2(F)@*meso*-SiO_2(P) and 10 min light exposure with 75 mW cm^{-2}.

treatments are shown in Fig. 6. While only some of the cells died after 2.5 min irradiation, all cells were killed after 10 min irradiation. In comparison, the cells subjected to laser irradiation in the absence of nanoparticles were kept intact.

3.5. Targeting delivery of PSs to cancer cells

The ability to target nanoparticles to specific organelles or receptors is one of the most important factors for their prospective application in bioimaging and drug delivery. Various types of targeting agents, such as antibodies, aptamers and folic acid, have been developed for the specific identification antigens or receptors on targeting cancer cells. In this study, folic acid was modified onto the Fe_3O_4@SiO_2(F)@*meso*-SiO_2(P) as the targeting component because folate receptors (FR) are overexpressed in many human cancerous cells.[42] After folate modification, the nanoparticles still displayed good dispersion in water and other buffers (Figure S4, ESI†). As shown in Figure S4b, ESI†, the size distribution of the Fe_3O_4@SiO_2(F)@*meso*-SiO_2(P)-Folate nanoparticles is about 59 nm, which was close to that of

Fe_3O_4@SiO_2(F)@*meso*-SiO_2(P) particles without the folate modification. In addition, the zeta potential (Figure S7, ESI†) of the Fe_3O_4@SiO_2(F)@*meso*-SiO_2(P)-Folate at PBS buffer (0.1 mol L^{-1}, pH 7.4) was about −8.98 mV, more negatively charged than that of Fe_3O_4@SiO_2(F)@*meso*-SiO_2(P) nanoparticles (−3.08 mV).

To evaluate the targeting recognition capability of Fe_3O_4@SiO_2(F)@*meso*-SiO_2(P)-Folate nanoparticles, human cervical carcinoma cell line HeLa was incubated with Fe_3O_4@SiO_2(F)@*meso*-SiO_2(P)-Folate nanoparticles for 8 h in PBS buffer. For comparison, HeLa cells were also incubated with Fe_3O_4@SiO_2(F)@*meso*-SiO_2(P) nanoparticles under otherwise identical conditions. After washing the cells with PBS to remove the unbound nanoparticles, the cellular-uptake characteristics were investigated by laser-scanning confocal microscopy and flow cytometry (excitation at $\lambda = 488$ nm for FITC). As shown in Fig. 7, although the cellular uptake of both nanoparticles was observed by the HeLa cells, the cells incubated with Fe_3O_4@SiO_2(F)@*meso*-SiO_2(P)-Folate (Fig. 7a, d) displayed stronger luminescence signals than the cells treated with Fe_3O_4@SiO_2(F)@*meso*-SiO_2(P) (Fig. 7e, h), suggesting that more folate-modified nanoparticles were uptaken by HeLa cells. In addition, flow cytometry analysis results also indicated that the cells incubated with Fe_3O_4@SiO_2(F)@*meso*-SiO_2(P)-Folate displayed high emission intensities (line 3 in Fig. 8a), whereas the emission intensities of HeLa cells treated with Fe_3O_4@SiO_2(F)@*meso*-SiO_2(P) were lower (line 2 in Fig. 8a). This observation can be explained by the high specific interaction between folic acid on the Fe_3O_4@SiO_2(F)@*meso*-SiO_2(P)-Folate and FR on HeLa cells, which may increase the uptake through folate receptor-mediated endocytosis.[43] Therefore, these results present strong evidence about the target effects of the Fe_3O_4@SiO_2(F)@*meso*-SiO_2(P)-Folate nanocomposites for HeLa cells.

Furthermore, the PDT effects of Fe_3O_4@SiO_2(F)@*meso*-SiO_2(P)-Folate and Fe_3O_4@SiO_2(F)@*meso*-SiO_2(P) nanoparticles on HeLa cells were compared. As shown in Fig. 8b, although the PDT effects were observed for both nanoparticles, folate-modified Fe_3O_4@SiO_2(F)@*meso*-SiO_2(P)-Folate nanoparticles killed the HeLa cells more effectively than Fe_3O_4@SiO_2(F)@*meso*-SiO_2(P) nanoparticles. After 5 min irradiation of the 660 nm laser (75 mW cm^{-2}), 60 ± 2.2% of the HeLa cells treated with the folate-modified nanoparticles were killed. In comparison, under the same conditions, only 30 ± 3.6% of the cells treated with Fe_3O_4@SiO_2(F)@*meso*-SiO_2(P) nanoparticles were killed. Fluorescence microscopic experiments (Figure S8, ESI†) also indicated that after 10 min irradiation, folate-modified Fe_3O_4@SiO_2(F)@*meso*-SiO_2(P) nanoparticles killed the HeLa cells more effectively (nearly 100%) than Fe_3O_4@SiO_2(F)@*meso*-SiO_2(P) nanoparticles (nearly 50%), suggesting the specific targeting capability of folic acid.

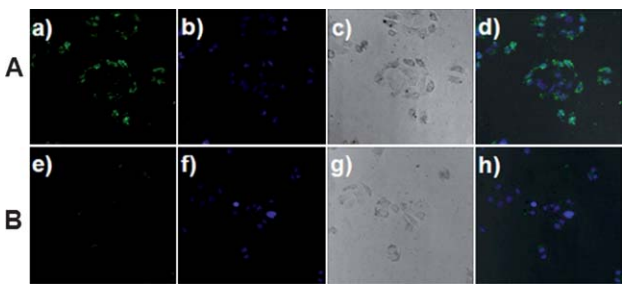

Fig. 7 Confocal fluorescence images showing the effect of folic acid modification on the nanoparticles (green fluorescence). The cell nuclei were stained with DAPI (blue fluorescence). HeLa treated with (A) Fe_3O_4@SiO_2(F)@*meso*-SiO_2(P)-Folate and (B) Fe_3O_4@SiO_2(F)@*meso*-SiO_2(P). The concentration of nanoparticles is 200 μg mL^{-1}. a) and e): nanoparticle fluorescence images, b) and f): DAPI fluorescence images, c) and g): bright- field images, d): merging of a), b) and c), h): merging of e), f) and g).

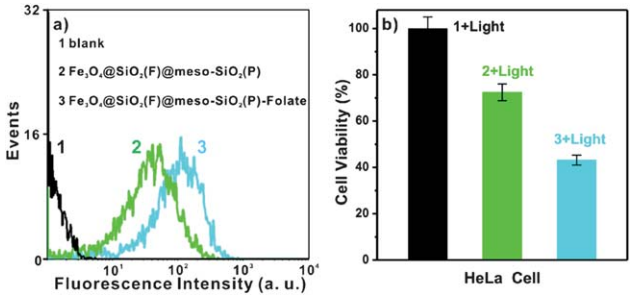

Fig. 8 a) Flow cytometry profiles of HeLa cells after being incubated with Fe_3O_4@SiO_2(F)@*meso*-SiO_2(P) and Fe_3O_4@SiO_2(F)@*meso*-SiO_2(P)-Folate for 8 h. Untreated HeLa cells were used as the control. 1, HeLa cells; 2, HeLa cells + Fe_3O_4@SiO_2(F)@*meso*-SiO_2(P); 3, HeLa cells + Fe_3O_4@SiO_2(F)@*meso*-SiO_2(P)-Folate. The concentration of nanoparticles was 200 μg mL^{-1}. b) MTT assay to demonstrate the phototoxic effect of the nanoparticles. HeLa cells were treated with Fe_3O_4@SiO_2(F)@*meso*-SiO_2(P) and Fe_3O_4@SiO_2(F)@*meso*-SiO_2(P)-Folate for 8 h, then irradiated with 660 nm laser for 5 min. The untreated cells with the same light irradiation were used as the control. The concentration of nanoparticles was 100 μg mL^{-1}.

4. Conclusions

In summary, multifunctional core-shell structured mesoporous silica nanoparticles with dual imaging and photosensitization capabilities were successfully fabricated. The encapsulation of a single magnetite nanoparticle and fluorescence dyes in one nonporous silica core endows the nanoparticles with the MRI and fluorescence imaging capabilities, allowing non-invasive tracking and monitoring of the nanoparticles within cells and even the body. The photosensitizer molecules (AlC_4Pc) covalently bound to the mesoporous silica shell exhibit a good stability against leaching and an excellent efficiency in photogenerating of reactive oxygen species. Furthermore, the surface modification of the core-shell nanoparticles by folic acid allows the targeted delivery of the PS to cancer cells and therefore minimizes the toxicity to the surrounding normal tissues. We have demonstrated the bioapplications of the multifunctional core-shell nanoparticles for MR and fluorescence imaging, and photodynamic therapy. *In vitro* studies indicated that these nanoparticles effectively killed cancer cells through the PDT process.

Acknowledgements

The work was financially supported by the NSFC (21021061, 20925103, 20871100), the Fok Ying Tung Education Foundation

(121011), NSF of Fujian Province for Distinguished Young Investigator Grant (2009J06005), the Fundamental Research Funds for the Central Universities (2010121015), and the Scientific Research Foundation for the Returned Overseas Chinese Scholars, State Education Ministry. We thank Professor Donghui Li of the Cancer Centre of Xiamen University for the supply of photosensitizers, AlC_4Pc, Dr Binghui Wu for help with the images and Dr Huaizhi Kang for help with revising the grammar.

References

1 D. E. J. G. J. Dolmans, D. Fukumura and R. K. Jain, *Nat. Rev. Cancer*, 2003, **3**, 380.
2 Y. N. Konan, R. Gruny and E. J. Allemann, *J. Photochem. Photobiol., B*, 2002, **66**, 89.
3 S. B. Brown, E. A. Brown and I. Walker, *Lancet Oncol.*, 2004, **5**, 497.
4 R. R. Allison, R. E. Cuenca, G. H. Downie, P. Camoitz, B. Brodish and C. H. Sibata, *Photodiagn. Photodyn. Ther.*, 2005, **2**, 205.
5 I. Roy, T. Y. Ohulchanskyy, H. E. Pudavar, E. J. Bergey, A. R. Oseroff, J. Morgan, T. J. Dougherty and P. N. Prasad, *J. Am. Chem. Soc.*, 2003, **125**, 7860.
6 K. Woodburn and D. Kessel, *J. Photochem. Photobiol., B*, 1994, **22**, 197.
7 B. Chen, B. W. Pogue and T. Hasan, *Expert Opin. Drug Delivery*, 2005, **2**, 477.
8 C. L. Peng, M. J. Shieh, M. H. Tsai, C. C. Chang and P. S. Lai, *Biomaterials*, 2008, **29**, 3599.
9 D. K. Chatterjee, L. S. Fong and Y. Zhang, *Adv. Drug Delivery Rev.*, 2008, **60**, 1627.
10 Y. Cheng, A. C. Samia, J. D. Meyers, I. Panagopoulos, B. Fei and C. Burda, *J. Am. Chem. Soc.*, 2008, **130**, 10643.
11 R. Bakalova, H. Ohba, Z. Zhelev, T. Nagase, R. Jose, M. Ishikawa and Y. Baba, *Nano Lett.*, 2004, **4**, 1567.
12 H. W. Gu, K. M. Xu, Z. M. Yang, C. K. Chang and B. Xu, *Chem. Commun.*, 2005, 4270.
13 J. Schwiertz, A. Wiehe, S. Gräfe, B. Gitter and M. Epple, *Biomaterials*, 2009, **30**, 3324.
14 D. B. Tada, L. L. R. Vono, E. L. Duarte, R. Itri, P. K. Kiyohara, M. S. Baptista and L. M. Rossi, *Langmuir*, 2007, **23**, 8194.
15 T. Y. Ohulchanskyy, I. Roy, L. N. Goswami, Y. H. Chen, E. J. Bergey, R. K. Pandey, A. R. Oseroff and P. N. Prasad, *Nano Lett.*, 2007, **7**, 2835.
16 X. X. He, X. Wu, K. M. Wang, B. H. Shi and L. Hai, *Biomaterials*, 2009, **30**, 5601.
17 P. Zhang, W. Steelant, M. Kumar and M. Scholfield, *J. Am. Chem. Soc.*, 2007, **129**, 4526.
18 G. F. Paciotti, D. G. I. Kingston and L. Tamarkin, *Drug Dev. Res.*, 2006, **67**, 47.
19 R. Liu, X. Zhao, T. Wu and P. Y. Feng, *J. Am. Chem. Soc.*, 2008, **130**, 14418.
20 K. Feng, R. Y. Zhang, L. Z. Wu, B. Tu, M. L. Peng, L. P. Zhang, D. Y. Zhao and C. H. Tung, *J. Am. Chem. Soc.*, 2006, **128**, 14685.
21 M. Vallt-Regi, F. Balas and D. Arcos, *Angew. Chem., Int. Ed.*, 2007, **46**, 7548.
22 I. I. Slowing, B. G. Trewyn, S. Giri and V. S. Y. Lin, *Adv. Funct. Mater.*, 2007, **17**, 1225.
23 Y. Wu, G. Cheng, K. Katsov, S. W. Sides, J. Wang, J. Tang, G. H. Fredrickson, M. Moskovits and G. D. Stucky, *Nat. Mater.*, 2004, **3**, 816.
24 J. Wang, C. Tsung, R. C. Hayward, Y. Wu and G. D. Stucky, *Angew. Chem., Int. Ed.*, 2005, **44**, 332.
25 J. Lu, M. Liong, J. I. Zink and F. Tamanoi, *Small*, 2007, **8**, 1341.
26 S. L. Gai, P. P. Yang, C. X. Li, W. X. Wang, Y. L. Dai, N. Niu and J. Lin, *Adv. Funct. Mater.*, 2010, **20**, 1166.
27 S. H. Cheng, C. H. Lee, C. S. Yang, F. G. Tseng, C. Y. Mou and L. W. Lo, *J. Mater. Chem.*, 2009, **19**, 1252.
28 H. S. Qian, H. C. Guo, P. C. L. Ho, R. Mahendran and Y. Zhang, *Small*, 2009, **5**, 2285.
29 R. R. Zhang, C. L. Wu, L. L. Tong, B. Tang and Q. H. Xu, *Langmuir*, 2009, **25**, 10153.
30 S. H. Cheng, C. H. Lee, M. C. Chen, J. S. Souris, F. G. Tseng, C. S. Yang, C. Y. Mou, C. T. Chen and L. W. Lo, *J. Mater. Chem.*, 2010, **20**, 6149.
31 M. F. Kircher, U. Mahmood, R. S. King, R. Weissleder and L. Josephson, *Cancer Res.*, 2003, **63**, 8122.
32 J. Michaelis, C. Hettich, J. Mlynek and V. Sandoghdar, *Nat. Med.*, 2000, **405**, 586.
33 H. A. Collins, M. Khurana, E. H. Moriyama, A. Mariampillai, E. Dahlstedt, M. Balaz, M. K. Kuimova, M. Drobizhev, V. X. D. Yang, D. Phillips, A. Rebane, B. C. Wilson and H. L. Anderson, *Nat. Photonics*, 2008, **2**, 420.
34 T. Hasan, *Photodynamic therapy: Basic principles and clinical applications*, Mercel Dekker, New York, 1992.
35 F. P. Chen and D. Y. Xu, *Chin. J. Org. Chem.*, 2005, **10**, 550.
36 S. H. Sun, H. Zeng, D. B. Robinson, S. Raoux, P. M. Rice, S. X. Wang and G. X. Li, *J. Am. Chem. Soc.*, 2004, **126**, 273.
37 W. StÖber, A. Fink and E. Bohn, *J. Colloid Interface Sci.*, 1968, **26**, 62.
38 J. W. Bulte and D. L. Kraitchman, *NMR Biomed.*, 2004, **17**, 484.
39 B. Z. Zhao, J. J. Yin, P. J. Bilski, C. F. Chignell, J. E. Roberts and Y. Y. He, *Toxicol. Appl. Pharmacol.*, 2009, **241**, 163.
40 E. A. Lukyanets, *J. Porphyrins Phthalocyanines*, 1999, **3**, 424.
41 W. Spiller, H. Kliesch, D. Wohrele, S. Hackbarth, B. Roder and G. J. Schnurpfeil, *J. Porphyrins Phthalocyanines*, 1998, **2**, 145.
42 N. W. S. Kam, M. O'Connell, J. A. Wisdom and H. Dai, *Proc. Natl. Acad. Sci. U. S. A.*, 2005, **102**, 11600.
43 R. J. Lee and P. S. Low, *J. Biol. Chem.*, 1994, **269**, 3198.

